

Electronic structure of $\text{Tb}_{0.5}\text{Sr}_{0.5}\text{MnO}_3$

T. Ly Nguyen,^{1,2} J. Rubio-Zuazo,^{3,4} G. R. Castro,^{3,4} F. M. F. de Groot,⁵ N. Hariharan,⁶ S. Elizabeth,⁶ M. Oura,⁷ Y. C. Tseng,^{1,8} H. J. Lin,² and A. Chainani^{2,7}

¹International College of Semiconductor Technology, National Yang Ming Chiao Tung University, Hsinchu 30010, Taiwan

²National Synchrotron Radiation Research Center, Hsinchu 30076, Taiwan

³Spanish CRG BM25-SpLine Beamline at the ESRF, 71 avenue des Martyrs 38000 Grenoble, France
and ESRF-The European Synchrotron CS 40220, 38043 Grenoble Cedex 09, France

⁴Instituto de Ciencia de Materiales de Madrid, CSIC, Cantoblanco, E-28049 Madrid, Spain

⁵Inorganic Chemistry and Catalysis, Utrecht University, Sorbonnelaan 16, 3584 CA Utrecht, Netherlands

⁶Department of Physics, Indian Institute of Science, Bangalore 560012, India

⁷RIKEN SPring-8 Center, Hyogo, Japan

⁸Department of Materials Science and Engineering, National Yang Ming Chiao Tung University, Hsinchu 30010, Taiwan



(Received 30 March 2021; accepted 27 May 2021; published 21 June 2021)

We study the electronic structure of single-crystal $\text{Tb}_{0.5}\text{Sr}_{0.5}\text{MnO}_3$, a non-charge-ordered mixed-valent semiconductor which exhibits a glassy magnetic ground state. We use the techniques of soft x-ray photoemission, hard x-ray photoemission, x-ray absorption, and resonant photoemission spectroscopy to investigate the occupied and unoccupied electronic states of $\text{Tb}_{0.5}\text{Sr}_{0.5}\text{MnO}_3$. Core level photoemission and x-ray absorption spectroscopy allow us to determine the valence states of Tb, Sr, and Mn ions in $\text{Tb}_{0.5}\text{Sr}_{0.5}\text{MnO}_3$. Model charge transfer multiplet calculations of core level photoemission and x-ray absorption spectra are employed to separate out the Mn^{3+} and Mn^{4+} states and confirm their relative concentrations. Resonant photoemission spectroscopy across the Mn $2p$ - $3d$ threshold shows clear resonant enhancement of the Mn $3d$ partial density of states and two-hole correlation satellites. A Cini-Sawatzky analysis gives on-site Coulomb energy $U_{dd} \sim 5.5 \pm 0.2$ eV for the Mn $3d^n$ states and $U_{pd} = 0.7$ eV ± 0.2 eV for the Mn $3d^{n+1}L^1$ states. The O $1s$ - $2p$ resonant photoemission is used to identify the O $2p$ two-hole correlation satellite which provides $U_{pp} \sim 3.4 \pm 0.2$ eV for the O $2p$ states. Valence band photoemission indicates a small-gap semiconductor (< 100 meV) consistent with electrical transport measurements. The estimated electronic structure parameters of the on-site Coulomb energies, in combination with the charge transfer energy and the hybridization strength obtained from the model calculations, indicate that $\text{Tb}_{0.5}\text{Sr}_{0.5}\text{MnO}_3$ is a strongly correlated charge transfer type semiconductor.

DOI: [10.1103/PhysRevB.103.245131](https://doi.org/10.1103/PhysRevB.103.245131)

I. INTRODUCTION

Perovskite manganite materials have been the subject of a very large number of studies because of their interesting physical properties such as colossal magnetoresistance (CMR); charge, orbital, and magnetic ordering [1–8]; and issues of phase separation [9–12]. The parent trivalent rare-earth manganese oxide $R^{3+}\text{Mn}^{3+}\text{O}_3^{2-}$ ($R=\text{La-Dy}$) and the divalent alkaline-earth manganese oxide $A^{2+}\text{Mn}^{4+}\text{O}_3^{2-}$ ($A=\text{Sr, Ba, Ca}$) are known to be antiferromagnetic insulators due to $\text{Mn}^{3+}\text{-O-Mn}^{3+}$ and $\text{Mn}^{4+}\text{-O-Mn}^{4+}$ superexchange interactions, respectively [13–19]. However, the electrical and magnetic properties of the mixed-crystal $R\text{MnO}_3$ - $A\text{MnO}_3$ show fascinating properties such as metal-insulator transitions, CMR, and various ordering behaviors driven by spin-charge-lattice coupling [20]. Since the first study more than 70 years ago which showed ferromagnetism in the three systems $\text{La}_{1-x}\text{Ca}_x\text{MnO}_3$, $\text{La}_{1-x}\text{Sr}_x\text{MnO}_3$, and $\text{La}_{1-x}\text{Ba}_x\text{MnO}_3$ over a certain range of compositions [21], extensive studies of the physical properties in mixed crys-

tals have been reported. The crystal structure of parent compounds LaMnO_3 and CaMnO_3 is orthorhombic, while for intermediate compositions, it becomes rhombohedral. For example, $\text{La}_{1-x}\text{Sr}_x\text{MnO}_3$ compounds are ferromagnetic metals for $0.1 < x < 0.5$ and become antiferromagnetic metals for $0.5 < x < 0.9$ [1–8,12,13,21]. The $\text{La}_{1-x}\text{Ca}_x\text{MnO}_3$ compounds with $0.2 < x < 0.5$ are also metallic ferromagnets but show charge ordered antiferromagnetism for $0.5 < x < 0.9$ [22–24]. Thus, as a function of x , in the compositions $\text{La}_{1-x}\text{A}_x\text{MnO}_3$, the average valence of Mn ions is changed from $3+$ ($x=0$) to $4+$ ($x=1$) by replacing La^{3+} ions in LaMnO_3 with A^{2+} ions, and simultaneously, the intermediate compositions exhibit a competition between ferromagnetic and antiferromagnetic orderings. However, surprisingly, the half-doped case with $x=0.5$ shows some differences in their physical properties depending on the A ion, although they possess an average Mn valence of 3.5. Namely, $\text{La}_{0.5}\text{Ca}_{0.5}\text{MnO}_3$ is a ferromagnetic insulator which shows charge order [22–24], while $\text{La}_{0.5}\text{Sr}_{0.5}\text{MnO}_3$ is ferromagnetic and metallic [25,26]. The origin of this difference is the size

mismatch between La^{3+} and A^{2+} , which randomly occupy the same crystallographic site [20]. On the other hand, in another set of experiments which investigated the dependence of the rare-earth R -ion sizes in the $R_{1-x}\text{A}_x\text{MnO}_3$ series, the materials showed unusual physical properties, as discussed in the following.

The RMnO_3 series with $R = \text{Gd}, \text{Tb},$ and Dy also contains antiferromagnetic insulators ($T_N = 44$ K) with an orthorhombic structure [27–29]. The Sr-substituted $R_{1-x}\text{Sr}_x\text{MnO}_3$ series shows systematic behavior as a function of x , and special attention was paid to the systems $\text{R}_{0.5}\text{Sr}_{0.5}\text{MnO}_3$. They are neither ferromagnetic and metallic nor antiferromagnetic and charge ordered but are magnetic glassy semiconductors [30]. This behavior is rather unusual compared to the spin-charge ordered manganites. Further, $\text{Tb}_{0.5}\text{Sr}_{0.5}\text{MnO}_3$ (TSMO50) was studied in detail for its dielectric, impedance, and transport properties as well as glassy magnetic properties by electrical and magnetic measurements [30,31]. The results showed that the temperature-dependent dielectric response exhibits frequency dispersion in the real (ϵ') and imaginary (ϵ'') parts of the dielectric constant and supports a thermally activated relaxation mechanism. Surprisingly, the results showed two relaxation regions separated by the glassy magnetic transition temperature ($T_g = 44$ K). The estimated activation energies of the dielectric permittivity above and below the glassy magnetic transition were 47 and 19 meV, respectively. On the other hand, the activation energy of the electrical resistivity between 80 and 300 K was estimated to be about 30 meV. Although the results ruled out a typical magneto-electric behavior, coupling between electric and magnetic properties could be confirmed for glassy TSMO50 [31].

While there have been several structural, electrical, and magnetic studies on TSMO50, as discussed above [27–31], no electronic structure studies of TSMO50 have been reported to date. Thus, we have carried out a detailed electron spectroscopic investigation of TSMO50 using the techniques of soft x-ray photoemission spectroscopy (SX-PES), hard x-ray photoemission spectroscopy (HAXPES), and x-ray absorption spectroscopy (XAS). We determine the oxidation state of the elements in TSMO50 through core level measurements. The core level Mn $2p$ PES, Mn $1s$ PES, and Mn L -edge XAS spectra were simulated by charge transfer multiplet (CTM) calculations using the CTM4XAS program for a MnO_6 cluster model with full atomic multiplets [32]. From valence band spectroscopy, we identify the Tb $4f$, Mn $3d$, and O $2p$ states. Our results confirm that TSMO50 exhibits a small semiconducting gap in the valence-band spectrum. Moreover, based on the Mn $2p$ - $3d$ and O $1s$ - $2p$ resonance photoemission spectroscopy, we observed Mn L_3VV and O KVV two-hole correlation satellites, which allow us to estimate the on-site Coulomb correlation energies in the Mn $3d$ and O $2p$ manifolds. The results show that TSMO50 is a strongly correlated charge transfer semiconductor.

II. SAMPLE PREPARATION, CHARACTERIZATION, AND EXPERIMENTAL DETAILS

TSMO50 single crystals were grown by the floating-zone technique using a four-mirror optical-image furnace. The quality of the TSMO50 was verified through x-ray Laue

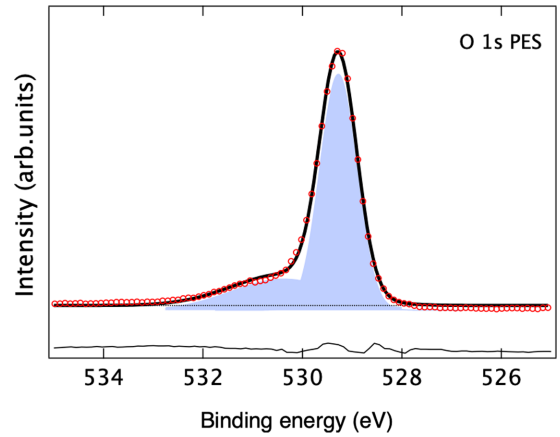


FIG. 1. The O $1s$ SX-PES core level spectrum (red circles) of TSMO50, measured using an incident photon energy $h\nu = 1200$ eV. The black line overlaid on the spectrum is a least-squares fit obtained using two Gaussian functions.

diffraction and the powder x-ray diffraction pattern of crushed single crystals using a Philips X'pert x-ray diffractometer with Cu K radiation, and the results confirmed a pure single phase. The electrical transport properties of TSMO50 single crystals were reported earlier [31], and it is a small-gap semiconductor at high temperatures with an activation energy of 30 (47) meV from resistivity (dielectric) permittivity. The SX-PES and XAS experiments were performed on a spectrometer with a total-energy resolution of 200 meV at BL17SU SPring-8 [33,34] using a Gammadata-Scienta SES2002 electron analyzer. The soft x-ray PES and XAS experiments were carried out using linear horizontal polarization of the incident photon beam. Samples were cleaved *in situ* and measured at $T = 300$ K under a base vacuum of 4×10^{-8} Pa. The energy calibration and resolution were determined from the Fermi-edge (E_F) spectrum of a gold film evaporated on the sample holder. The core level SX-PES data were obtained in the angle-integrated mode with an incident photon energy $h\nu = 1200$ eV. Resonant PES spectra were measured across the Mn $2p$ - $3d$ and O $1s$ - $2p$ thresholds, and the spectra were normalized for scan time and incident photon flux. XAS was recorded in the total electron yield mode. HAXPES spectra were measured at branch B of the BM25-SpLine beamline at the European Synchrotron Radiation Facility (ESRF). The HAXPES measurements were done with an incident photon energy $h\nu = 14$ keV, obtained using a Si(111) double-crystal monochromator, with an energy resolution of 1.6 eV measured using the Fermi edge of Pd metal. HAXPES measurements were carried out in a vacuum of 4 – 6×10^{-8} Pa. The Mn $1s$ HAXPES was carried out at $T = 300$ K and $T = 80$ K, while the Sr $2s$ and Tb $2p$ measurements were carried out at $T = 300$ K.

III. RESULTS AND DISCUSSION

The SX-PES of the O $1s$ core level spectrum measured with an incident photon energy $h\nu = 1200$ eV is shown in Fig. 1. The spectrum was fitted using two Gaussian functions to determine the peak positions. It shows a main peak at

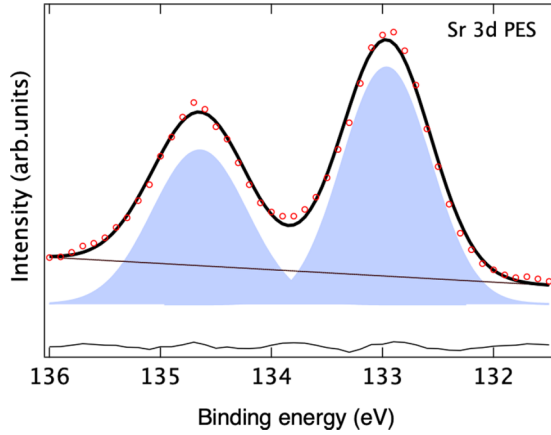


FIG. 2. The Sr $3d$ SX-PES core level spectrum (red circles) of TSMO50, measured using an incident photon energy $h\nu = 1200$ eV. The black line overlaid on the spectrum is a least-squares fit obtained using two Gaussian functions.

529.28 eV binding energy (BE) with a FWHM of 0.9 eV and a weak secondary structure at 530.34 eV. The main peak BE is typical of transition metal oxides. For example, the O $1s$ main peak of MnO is observed at a BE of 529.25 eV [35,36]. The weak secondary structure seen in TSMO50 was also observed for cleaved surfaces of transition metal monoxides like MnO, FeO, and CoO single crystals and is attributed to oxygen nonstoichiometry [35].

Figure 2 shows the Sr $3d$ SX-PES core level spectrum measured with an incident photon energy $h\nu = 1200$ eV. The spectrum consists of two peaks which correspond to the spin-orbit split $3d_{5/2}$ and $3d_{3/2}$ features. The peaks are positioned at BEs of 132.95 eV ($3d_{5/2}$, with FWHM of 0.9 eV) and 134.65 eV ($3d_{3/2}$ with FWHM of 1.0 eV), respectively. The BEs of the Sr $3d$ features confirm the divalent states of Sr ions in TSMO50. It is noted that the Sr $3d$ SX-PES spectra show no satellites. Based on a least squares fitting of the spectrum, the areas of the two peaks are found to be in the ratio 3:2 corresponding to $3d_{5/2}$ and $3d_{3/2}$ states, consistent with the expected degeneracy of the spin-orbit split features.

Mn $2p$ SX-PES of TSMO50 measured with a photon energy of $h\nu = 1200$ eV is shown in Fig. 3. The spectrum shows two main peaks corresponding to the spin-orbit split $2p_{3/2}$ and $2p_{1/2}$ doublet states with binding energies of 643.18 and 654.72 eV, respectively, and an energy separation of 11.54 eV. The spectra are similar to SX-PES spectra reported for $\text{La}_{1-x}\text{Sr}_x\text{MnO}_3$ [37–41]. A broad, weak-intensity satellite feature is obtained at about 9–11 eV above the main $2p_{1/2}$ core level, and it is ascribed to the poorly screened final state. This observation implies that the expected satellite feature of the $2p_{3/2}$ level overlaps and gets mixed with the $2p_{1/2}$ main peak [37]. Since the chemical formula of stoichiometric TSMO50 implies a 1:1 ratio of $\text{Mn}^{3+}:\text{Mn}^{4+}$, in order to separate out their respective contributions to the Mn $2p$ spectrum, we have simulated the Mn^{3+} $2p$ SX-PES (blue curve) and Mn^{4+} $2p$ SX-PES (green curve) spectra using model cluster calculations. We used the CTM program [32] to carry out model cluster calculations, including atomic multiplets and charge-transferred states to simulate the experimental spectra. In the

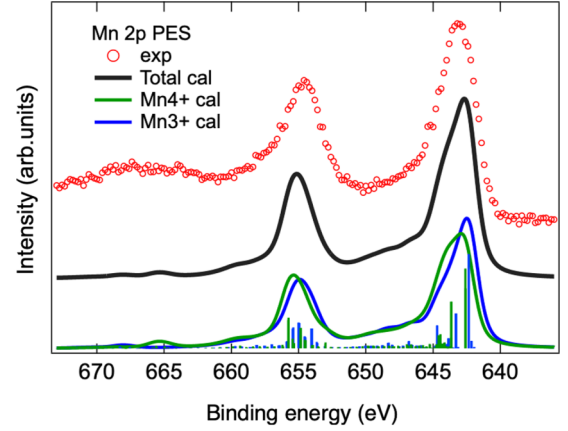


FIG. 3. The experimental Mn $2p$ SX-PES core level spectrum (red circles) of TSMO50, measured using an incident photon energy $h\nu = 1200$ eV and compared with a calculated total spectrum (black line) obtained using a charge transfer multiplet calculation. The total calculated spectrum is obtained by adding the calculated spectra for Mn^{3+} and Mn^{4+} configurations in a 1:1 ratio.

present case, for the Mn^{3+} configuration, we use d^4 and $d^5\bar{L}^1$ basis states, where \bar{L}^1 represents a symmetry-adapted ligand hole state. Similarly, for the Mn^{4+} configuration, we use d^3 and $d^4\bar{L}^1$ basis states. The initial state and final states can then be described as a linear combination of the d^n and $d^{n+1}\bar{L}^1$ basis states. Further details of the calculation method are described in Refs. [32,42,43]. The Slater integrals were reduced to 0.8 compared to the Hartree-Fock values. A fair match to the experimental spectrum was obtained using the electronic structure parameters for Mn^{3+} and Mn^{4+} , as shown in Table I. The black curve in Fig. 3 is obtained by adding the Mn^{3+} $2p$ SX-PES and Mn^{4+} $2p$ SX-PES calculations with a 1:1 ratio. In an earlier study on $\text{La}_{0.67}\text{Pb}_{0.33}\text{MnO}_3$, the authors estimated a $\text{Mn}^{3+}/\text{Mn}^{4+}$ ratio of 2:1 using Mn $2p$ SX-PES [44,45]. Since the estimated on-site Coulomb energy U_{dd} is larger than the charge transfer energy Δ , defined as the energy difference between the $3d^n$ and $3d^{n+1}\bar{L}^1$ states, the results indicate that TSMO50 is a strongly correlated charge transfer type material with the lowest energy excitation corresponding to a p - d type excitation. In comparison, for the electronic parameters of $\text{La}_{0.66}\text{Ca}_{0.33}\text{MnO}_3$ using a cluster model without atomic multiplets, Zalecki *et al.* estimated values of $U_{dd} = 6.4$ eV and $\Delta = 3.5$ eV [46]. On the other hand, Hong *et al.* estimated the so-called soft x-ray fluorescence charge transfer energy

TABLE I. Parameters used for the Mn $2p$ PES, Mn $1s$ HAX-PES, and Mn L -edge XAS calculation: on-site Coulomb energy U_{dd} between two d valence electrons, the Coulomb energy U_{cd} between the core hole and valence d electron, charge transfer energy Δ , hybridization strengths T_{eg} and T_{t2g} , crystal field splitting energy $10D_q$, and the number of d electrons n_d .

	U_{dd} (eV)	U_{cd} (eV)	Δ (eV)	T_{eg} (eV)	T_{t2g} (eV)	$10D_q$ (eV)	n_d electrons
Mn^{3+}	5.5	6.5	1.0	3.2	1.6	1.5	4.49
Mn^{4+}	5.5	6.5	0.0	2.0	1.0	2.6	3.52

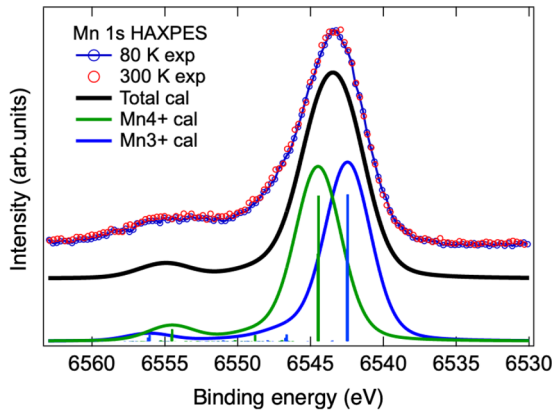


FIG. 4. The experimental Mn $1s$ HAXPES spectra of TSMO50, measured using an incident photon energy $h\nu = 14$ keV at low temperature ($T = 80$ K) and room temperature ($T = 300$ K), show negligible changes. A comparison with a calculated total spectrum (black line) obtained using a charge transfer multiplet calculation reproduces the experimental spectrum. The total calculated spectrum is obtained by adding the calculated spectra for Mn^{3+} and Mn^{4+} configurations in a 1:1 ratio.

(SXF-CT), which equals Δ' , and the soft x-ray fluorescence band gap (SXF band gap) using O K -edge x-ray emission spectroscopy (XES) and XAS spectra for the series LaMO_3 ($M = \text{Cr, Mn, Fe, Co, Ni}$) [47]. For LaMnO_3 , the authors reported values of $(\text{SXF-CT}) = \Delta' \sim 5$ eV and a SXF band gap of 2.5 eV, but it was explained that these values are necessarily larger than the physical values of Δ and the actual band gap, because Δ' was the energy difference between the peak DOS energies in O K -edge XES and XAS spectra [47].

We carried out Mn $1s$ core level HAXPES measurements of TSMO50 at $T = 300$ K (red circles) and $T = 80$ K (blue circles), as shown in Fig. 4. The spectra show a main peak at 6543.3 eV and a broad satellite feature around 6553 eV but do not show any temperature dependence. We also applied the CTM4XAS program to calculate the Mn^{3+} $1s$ HAXPES and Mn^{4+} $1s$ HAXPES spectra with the same parameters as presented in Table I. In Fig. 4, we plot the sum of Mn^{3+} $1s$ and Mn^{4+} $1s$ calculated spectra (black curve) in a 1:1 ratio together with the experimental spectra. This comparison shows reasonable agreement between the calculated spectrum and the experimental spectra, thereby confirming the nominal ratio of 1:1 trivalent and tetravalent manganese ions in TSMO50. It is noted that the spectra do not show a low binding energy well-screened peak in Mn $1s$ HAXPES core level spectra of TSMO50. This result is consistent with the fact that TSMO50 is a semiconductor, in contrast to the Mn $2p$ and Mn $1s$ of $\text{La}_{1-x}\text{Sr}_x\text{MnO}_3$, with $x = 0.2-0.4$, which shows a well-screened peak on the low binding energy side of the main peak in the low-temperature metallic phase [39–41, 48–50].

The Sr $2s$ and Tb $2p_{3/2}$ HAXPES core level spectra are shown in Figs. 5 and 6, respectively. Both spectra show a broad single-peak feature. The Sr $2s$ peak has a BE of 2215.2 eV with FWHM of 5.94 eV, while the Tb $2p_{3/2}$ peak has a BE of 7518.6 eV with FWHM of 7.17 eV. The single-peak spectra obtained here are indicative of a well-defined Sr^{2+} and Tb^{3+} in TSMO50.

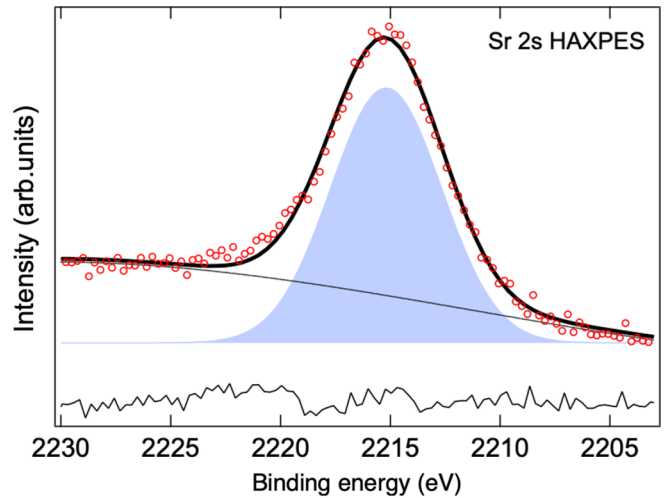


FIG. 5. The Sr $2s$ HAXPES of TSMO50 measured using an incident photon energy $h\nu = 14$ keV. The black line overlaid on the spectrum is a least-squares fit obtained using a Gaussian function.

The Mn L -edge XAS spectrum of TSMO50 is shown in Fig. 7(a) with two broad peaks corresponding to the spin-orbit split $L_3(2p_{3/2})$ and $L_2(2p_{1/2})$ states. The L_3 edge consists of a main peak at 642.83 eV and a shoulder at 640.9 eV. The Mn L_2 edge consists of a main peak at 653.51 eV and a shoulder at 651.60 eV. By comparing the present Mn $2p$ XAS spectrum with reference manganese oxides [51], the peak positions and the line shapes of TSMO50 are similar to $\text{SrMn}_{1-x}\text{Mo}_x\text{O}_3$, which consists of a combination of trivalent Mn^{3+} and tetravalent Mn^{4+} states. This similarity is confirmed by CTM calculations for the Mn^{3+} and Mn^{4+} XAS spectra obtained using the same electronic parameters as Mn $2p$ XPS shown in Fig. 3. The combination of Mn^{3+} L -edge and Mn^{4+} L -edge calculations in a 1:1 ratio exhibits a shape very similar to the experimental Mn L -edge spectrum. These results confirm the presence of Mn^{3+} and Mn^{4+} states consistent with the nominal chemical formula of this material.

We next performed the Mn $2p$ - $3d$ (L -edge) resonant PES at photon energies labeled A–R, as shown in Fig. 7. The

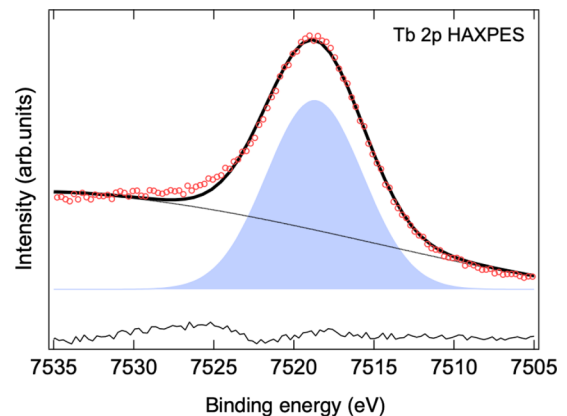


FIG. 6. The Tb $2p_{3/2}$ HAXPES of TSMO50 measured using an incident photon energy $h\nu = 14$ keV. The black line overlaid on the spectrum is a least-squares fit obtained using a Gaussian function.

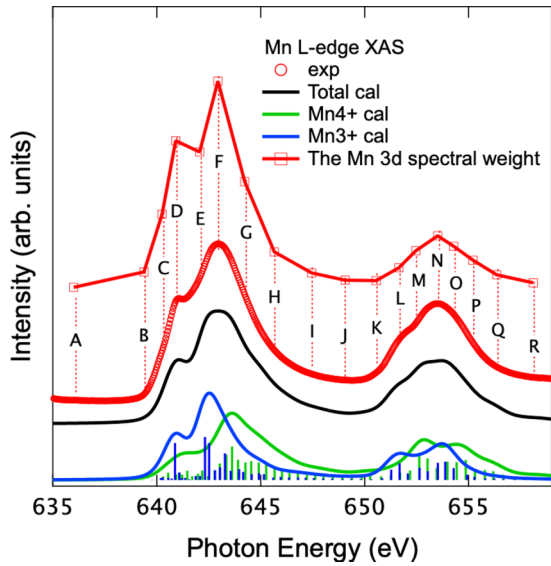


FIG. 7. Experimental Mn L -edge XAS spectrum (red circles) of TSMO50 compared with the total calculated spectrum (black line) obtained using the CTM calculations for the Mn^{3+} (blue line) and Mn^{4+} (green line) configurations, added in a 1:1 ratio. The Mn $3d$ spectral weight between binding energies of 0 and 3 eV obtained from the Mn $2p$ - $3d$ resonant valence band photoemission spectra (Fig. 8) is also plotted for comparison.

Mn L_3 -edge and L_2 -edge resonant PES spectra are shown in Figs. 8(a) and 8(b), respectively. The spectra show several features with the valence band states positioned between E_F and about 12 eV BE. We first discuss the assignments of weak shallow core level features between ~ 17 and 24 eV BE. A weak doublet feature at 17.7 and 18.7 eV BE corresponds to the Sr $4p_{3/2}$ and $4p_{1/2}$ states [52]. The feature at 20.5 eV BE corresponds to the main multiplet feature of Tb $5p$ [53]. The higher multiplet feature of Tb $5p$ is known to occur at ~ 2 eV higher BE and overlaps with the O $2s$ feature at ~ 23.3 eV BE [52,53]. These shallow core level features are marked by gray dotted lines in Figs. 8(a) and 8(b) and are better seen on the expanded y scale in Fig. 11(a) below. Further, the intensity between 7 and 11 eV BE mainly corresponds to the Tb $4f$ multiplet states, while the feature at 6 eV BE is attributed the O $2p$ band. The character of the Tb $4f$ multiplet features has been confirmed by Tb $3d$ - $4f$ on-resonance data shown in Fig. 11 below and discussed later.

As we increase the photon energy from A to F across the Mn L_3 -edge threshold [Fig. 8(a)], we observe a systematic increase in the spectral intensity of the feature at ~ 2 eV BE in the valence band. For higher photon energies above F and up to J, the spectral intensity of the feature at ~ 2 eV decreases on increasing the photon energy. In Fig. 7, we have also plotted the Mn $3d$ spectral weight between E_F and 3 eV BE obtained from the Mn $2p$ - $3d$ resonant valence band photoemission spectra shown in Fig. 8. The maximum intensity observed at photon energy F matches the maximum of the XAS L_3 -edge intensity in Fig. 7. This indicates that the ~ 2 eV feature undergoes a resonance maximum of the Mn $3d$ partial density of states (DOS) associated with the L_3 edge. On increasing the photon energies further from J to R [Fig. 8(b)], we observe

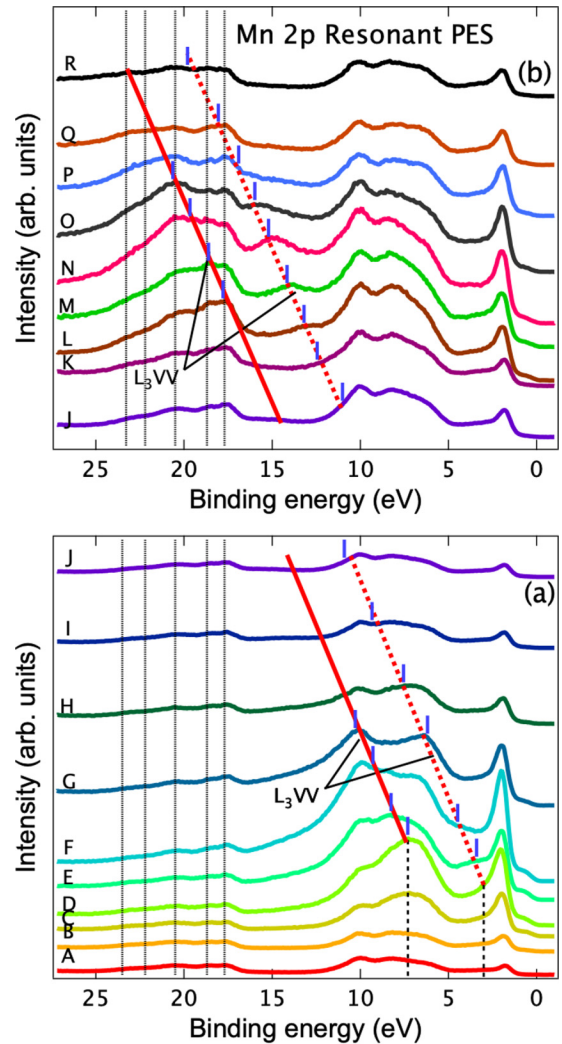


FIG. 8. The Mn $2p$ - $3d$ resonant photoemission spectroscopy of TSMO50 across $L_{2,3}$ edges obtained using photon energies labeled A to R in Fig. 7. The spectral peak intensities marked with red (solid and dotted) lines identify and show the systematic change of two L_3VV Auger features, as described in the text.

another maxima in the ~ 2 eV BE feature corresponding to the L_2 -edge resonance maximum.

In addition to the ~ 2 eV resonant feature, we could also observe large enhancement between 5 and 12 eV BE for photon energies C to G and between 17 and 25 eV BE for photon energies L to O. Further, we also see a clear satellite for photon energies L ($h\nu = 651.64$ eV) to O (654.28 eV) which systematically shifts to higher binding energies from 13 to 15.7 eV BE, as marked in Fig. 8(b) with a red dotted line and blue tick marks. Since this feature tracks the changes in the photon energy, it is attributed to an L_3VV Auger feature of Mn $3d$ character in the valence band DOS. In order to better see the evolution of this Auger feature we plot the difference spectra for photon energies B to G (with respect to spectrum A) and for photon energies L to O (with respect to spectrum J) in Figs. 9(a) and 9(b), respectively. The spectral peak intensities marked with red (solid and dotted) lines identify and show the systematic change in two L_3VV Auger features for photon energies from D to G and L to O. Accordingly, we

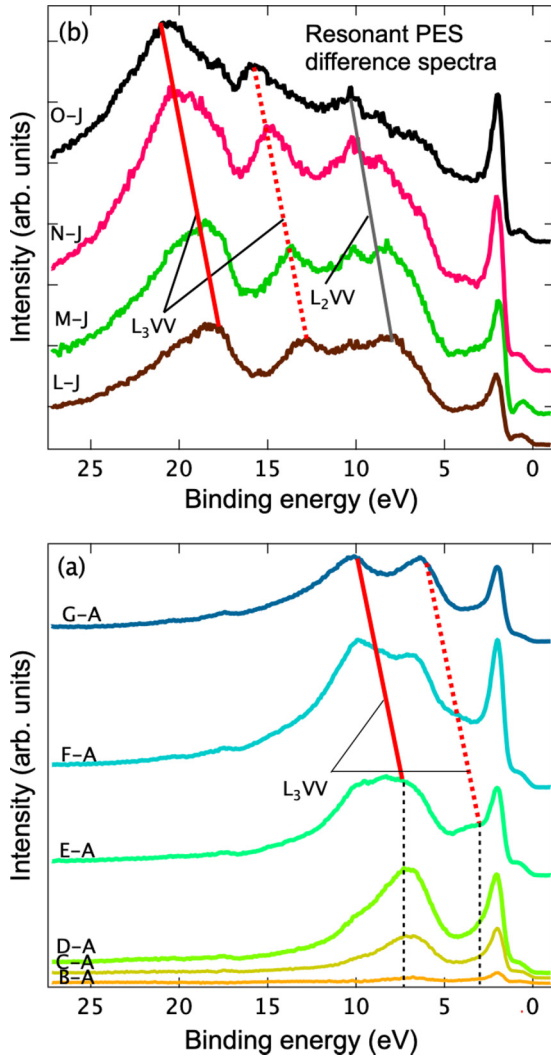


FIG. 9. The Mn $2p$ - $3d$ resonant photoemission difference spectra for (a) photon energies labeled B to G (with respect to spectrum A) and (b) photon energies labeled L to O (with respect to spectrum J). The spectral peak intensities marked with red (solid and dotted) lines identify and show the systematic change in two L_3VV Auger features.

have marked the L_3VV Auger features in Figs. 8(a) and 8(b), as shown by the red lines and blue tick marks. Similarly, we see another feature in Fig. 9(b) marked by the gray solid line which is assigned to the weaker L_2VV Auger feature.

In earlier studies on $\text{Nd}_{0.5}\text{A}_{0.5}\text{MnO}_3$ ($A=\text{Ca}, \text{Sr}$) [54] and $\text{LaMn}_{0.85}\text{Co}_{0.15}\text{O}_3$ [55], the Mn $2p$ - $3d$ on-resonant photoemission spectra were reported to show a very broad continuous L_3VV Auger feature spread from 6 to 16 eV. In contrast, our results show two well-separated L_3VV Auger features in Fig. 9. Following earlier work on the prototypical charge transfer insulator NiO [56], the high-BE L_3VV Auger feature is assigned to the mainly Mn d^n states (red solid lines in Figs. 8 and 9), and the low-BE L_3VV Auger feature is due to mainly $d^{n+1}\underline{L}^1$ states (red dotted lines in Figs. 8 and 9). Using the Cini-Sawatzky method [57–61], we can estimate the on-site Coulomb energy for the Mn $3d$ states U_{dd} from the Auger features. We use the equation

TABLE II. The BE of the $d^n L_3VV$ Auger peak E_{LVV} , the incident photon energy $h\nu$, the energy of the Mn $3d$ main peak ϵ_{3d} , the BE of the Mn $2p$ main peak E_{2p} , and the on-site Coulomb energy U_{dd} .

E_{LVV} (eV)	$h\nu$ (eV)	ϵ_{3d} (eV)	E_{2p} (eV)	U_{dd} (eV)
L=17.9	651.6	2.0	643.2	5.5
M=18.7	652.5	2.0	643.2	5.4
N=20.0	653.5	2.0	643.2	5.7
O=20.6	654.3	2.0	643.2	5.5

$U_{dd} = E_{2p} - (h\nu - E_{LVV}) - 2\epsilon_{3d}$ [62], where E_{2p} is the BE of the Mn $2p$ main peak (643.18 eV), $h\nu$ is the incident photon energy, and E_{LVV} corresponds to BE of the d^n Auger peak. In the equation, $2\epsilon_{3d}$ represents the average two-hole energy without correlations and is obtained as a self-convolution of the Mn $3d$ partial density of states with a main peak position of $\epsilon_{3d} = 2$ eV. From spectra obtained using photon energies labeled L–O, we estimate the on-site $U_{dd} = 5.5 \pm 0.2$ eV (see Table II) for the Mn d^n character L_3VV Auger feature. For the $d^{n+1}\underline{L}^1 L_3VV$ Auger feature at a BE of E'_{LVV} , while an interpretation in terms of an on-site Coulomb energy is not strictly valid, it could be considered to be a measure of an intersite Coulomb energy U_{pd} [63]. Thus, a corresponding Cini-Sawatzky analysis gives us a $U_{pd} = 0.7 \text{ eV} \pm 0.2 \text{ eV}$ (see Table III), indicative of weak p - d correlations in the strongly hybridized charge-transferred $d^{n+1}\underline{L}^1$ states. In comparison, for La_2CuO_4 , based on a three-band Hubbard model [63], Werner *et al.* estimated values of the static $U_{dd}(\omega = 0) = 7.0$ eV and $U_{pd}(\omega = 0) = 1.88$ eV. The authors also estimated an on-site Coulomb energy $U_{pp}(\omega = 0) = 4.64$ eV for the O $2p$ states. We also carried out a Cini-Sawatzky analysis to determine the on-site Coulomb energy for the oxygen $2p$ states by measuring the O K -edge XAS and O $1s$ - $2p$ resonant valence band PES (Fig. 10). We obtain a value of $U_{pp} = 3.4 \pm 0.2$ eV, as discussed in the following.

Figure 10(a) shows the O $1s$ - $2p$ (K -edge) XAS spectrum of TSMO50. It exhibits a main peak at 529.45 eV, followed by a weak feature at 531.86 eV and two broad features centered at 535.98 and 543.46 eV. The 529.45 eV main peak, which actually consists of two features, as seen in the inset, is attributed to O $2p$ states hybridized with Mn $3d$ states, while the features at higher photon energies are due to O $2p$ states hybridized with Sr $4d$ and Tb $5d$ states. We then performed O $1s$ - $2p$ resonant PES using photon energies labeled A–D in Fig. 10(a),

TABLE III. The BE of the $d^{n+1}\underline{L}^1 L_3VV$ Auger peak E'_{LVV} , the incident photon energy $h\nu$, the energy of the Mn $3d$ main peak ϵ_{3d} , the BE of the Mn $2p$ main peak E_{2p} , and the intersite Coulomb energy U_{pd} .

E'_{LVV} (eV)	$h\nu$ (eV)	ϵ_{3d} (eV)	E_{2p} (eV)	U_{pd} (eV)
L=13.2	651.6	2.0	643.2	0.8
M=14.0	652.5	2.0	643.2	0.7
N=15.0	653.5	2.0	643.2	0.7
O=15.7	654.3	2.0	643.2	0.6

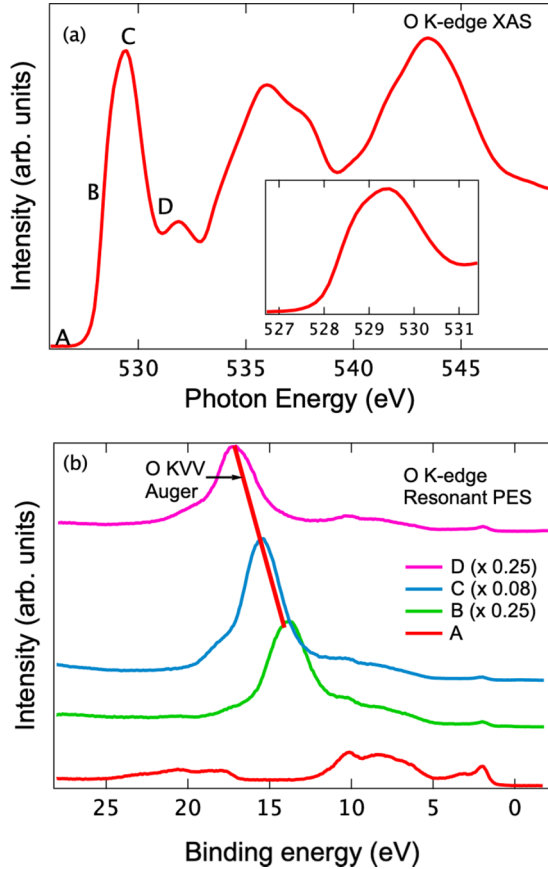


FIG. 10. (a) The O K -edge XAS spectrum of TSMO50. (b) The O K -edge resonant PES is measured by using photon energy determined by A–D in (a).

and the obtained spectra are shown in Fig. 10(b). While the O $2p$ partial DOS does not show a resonant enhancement, we see a resonance feature at higher BEs which tracks the increase in the photon energies [Fig. 10(b)]. Since it tracks the photon energy, it indicates that the feature is an O KVV Auger feature originating in the O $2p$ correlations in the valence band. Based on the equation $U_{pp} = E_{1s} - (hv - E_{KVV}) - 2\epsilon_{2p}$, the on-site Coulomb energy in the O $2p$ state is estimated to be $U_{pp} = 3.4 \pm 0.2$ eV, where $E_{1s} = 529.28$ eV is obtained from Fig. 1 and $\epsilon_{2p} = 6$ eV is the binding energy of the O $2p$ states estimated from valence band spectra shown in Fig. 11. Since, photon energy B ($hv = 528.81$ eV) lies about 0.5 eV below the O $1s$ core level BE ($hv = 529.28$ eV), the satellite feature seen in the spectrum obtained with photon energy B lies in the resonant Raman regime [62]. Hence, we have estimated U_{pp} for spectra obtained using only photon energies C and D (see Table IV).

This U_{pp} value is considerably smaller than U_{pp} values estimated for many oxides which showed $U_{pp} = 5$ –7 eV [37,64–71]. In fact, perovskite oxides of the RMO_3 type (where R is rare earth and M is transition metal) have shown a large U_{dd} of 4 to 6 eV and also a large U_{pp} of 5 to 7 eV [64–68]. Thus, in contrast to other perovskite oxides as well as other transition metal compounds like VO_2 , V_2O_3 , and high- T_c cuprates, TSMO50 shows a $U_{dd} = 5.5 \pm 0.2$ eV, comparable to or slightly larger than earlier estimates from Mn compounds, while $U_{pp} = 3.4 \pm 0.2$ eV is smaller than that

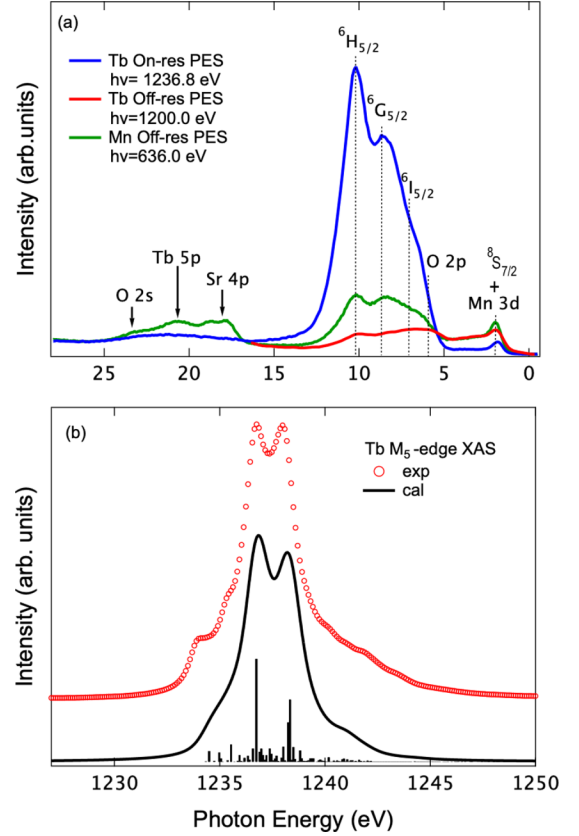


FIG. 11. (a) The valence band PES of TSMO50 measured at incident photon energies of $hv = 636$ eV (spectrum A of Fig. 8), $hv = 1200$ eV (Tb off resonance), and $hv = 1236.8$ eV (Tb on resonance). (b) Experimental Tb M_5 -edge XAS spectrum of TSMO50 compared with an atomic multiplet calculation.

estimated for other oxides. The present results suggest that this smaller value of U_{pp} may be an important characteristic of TSMO50 which does not exhibit charge or magnetic ordering with a $Mn^{3+}:Mn^{4+}$ ratio of 1:1, while $La_{0.5}Ca_{0.5}MnO_3$, $Nd_{0.5}Sr_{0.5}MnO_3$, etc., show spin, charge, and orbital ordering phenomena. Theoretical studies have also shown that strong on-site Coulomb interactions are the main requirement of charge ordering in the half-filled manganites [72–74]. In fact, most of the high- T_c cuprates have shown charge ordering with U_{dd} and U_{pp} both being large, ~ 5 to 7 eV [69–71]. The only exception of a small U_{pp} is the highest- T_c cuprate $HgBa_2Ca_2Cu_3O_{8+\delta}$ ($T_c = 134$ K), for which it was recently shown that $U_{dd} \sim 6.5$ eV and $U_{pp} \sim 1$ eV [75].

Here we would like to clarify that while the Cini-Sawatzky method has been reliably used to estimate on-site element-

TABLE IV. The BE of the Auger peak E_{KVV} , the incident photon energy hv , the energy of the O $2p$ main peak ϵ_{2p} , the BE of the O $1s$ main peak E_{1s} , and the on-site Coulomb energy U_{pp} .

E_{KVV} (eV)	hv (eV)	ϵ_{2p} (eV)	E_{1s} (eV)	U_{pp} (eV)
C=15.4	529.4	6.0	529.3	3.3
D=17.2	531.0	6.0	529.3	3.5

specific Coulomb correlation energies in several $3d$ transition metal (Ti to Cu) compounds [37,57–62,64–71], it is important to note that the on-site Coulomb correlation energy estimated using Auger spectra $U_{dd(\text{Auger})}$ is not exactly the same as the average on-site Coulomb energy used in the Hubbard model $U_{dd(\text{Hubbard})}$. $U_{dd(\text{Auger})}$ is defined as the energy cost in going from $2M^+ \rightarrow M + M^{2+}$, where M is an atom in a solid. Hence, $U_{dd(\text{Auger})}$, the Coulomb correlation energy between two valence holes, is the difference between the first ionization energy I_1 and second ionization energy I_2 , i.e., $U_{dd(\text{Auger})} = I_2 - I_1$. This is expected to be slightly different from $U_{dd(\text{Hubbard})}$, which corresponds to the energy cost of $2M \rightarrow M^- + M^+$ and $U_{dd(\text{Hubbard})} = I_1 - A$; that is, it is the difference between the first ionization energy I_1 and the electron affinity A . While both values correspond to the difference in energy between one less electron and one more electron compared to a reference state, the reference states are M and M^+ , respectively. These states are obviously not equal, but the difference in the estimated values of $U_{dd(\text{Auger})}$ and $U_{dd(\text{Hubbard})}$ is expected to be small due to screening effects in a solid [76]. For the cluster model calculations used in the present case, we have used a value of $U_{dd} = 5.5$ eV and have explicitly included the crystal field splitting $10Dq$ to describe t_{2g} - e_g splitting in the d -electron states. As discussed earlier, the initial and final states are described using only two basis states, d^n and $d^{n+1}\underline{L}^1$. In the final states of the core level PES and XAS calculations, since U_{dd} and U_{cd} occur only as $\Delta - U_{cd}$ and $\Delta + U_{dd} - U_{cd}$, respectively, the absolute value of U_{dd} is only indirectly present in the model [32,42,43]. The fair match of the calculations with the PES and XAS experimental results using the same electronic parameters validates the calculation procedure. It is known that orthorhombic DyMnO_3 shows a clear x-ray linear dichroism due to strong orbital polarization associated with magnetic and orbital ordering [77]. While TSMO50 does not show long-range magnetic or charge ordering, it may still show some linear dichroism due to short-range order. Thus, the weak deviations between experiment and calculations are possibly related to the use of linear horizontal polarization for the soft x-ray PES and XAS measurements.

Figure 11(a) shows the wide valence band PES of TSMO50 measured at incident photon energies $h\nu = 636, 1200,$ and 1236.8 eV to identify all the valence and shallow core states in TSMO50. The spectra are normalized for the background at high BE where there are no spectra features. The last two energies, 1200 and 1237 eV, are the off-resonant and on-resonant energies corresponding to the Tb $3d$ - $4f$ threshold. The Tb $3d$ - $4f$ off- and on-resonant incident photon energies were determined by first measuring the Tb $3d$ - $4f$ (M_5 -edge) XAS spectrum. The Tb $3d$ - $4f$ (M_5 -edge) XAS spectrum is shown in Fig. 11(b), along with atomic multiplet calculations using the CTM4XAS program. The Slater integral was reduced to 0.64 times the Hartree-Fock value to get the best match of the calculation with the experiment. The results confirm that Tb ions are trivalent in TSMO50. Thus, we chose an incident photon energy of $h\nu = 1236.8$ eV to correspond to the Tb $3d$ - $4f$ resonant energy and $h\nu = 1200$ eV to correspond to the off-resonant energy. The valence band spectra measured with the three different photon energies help us to identify the Mn $3d$, O $2p$, and Tb $4f$ partial DOSs in the valence band and the shallow core Sr $4p$, Tb $5p$, and O $2s$. In particular the

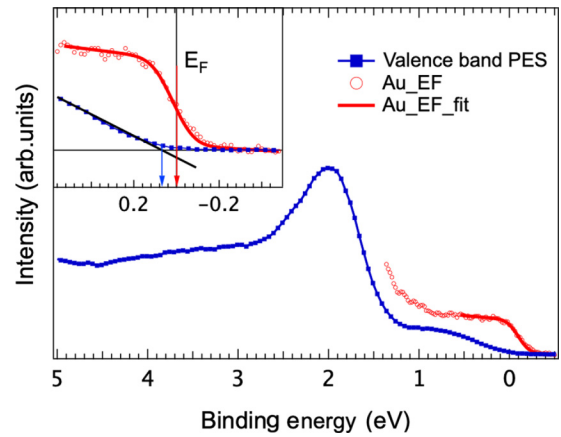


FIG. 12. Valence band PES of TSMO50 obtained using the photon energy $h\nu = 642.06$ eV (spectrum E of Fig. 8) compared with the Fermi edge of the gold reference sample. The inset shows the spectra near E_F plotted on an expanded scale.

Mn $3d$ partial DOS occurs between the Fermi level and ~ 4 eV BE; the Tb states are positioned at ~ 10.2 eV (${}^6\text{H}_{5/2}$), ~ 8.6 eV (${}^6\text{G}_{5/2}$), and ~ 7 eV (${}^6\text{I}_{5/2}$) BE [78,79], and the O $2p$ states are centered at about 6 eV BE. We have carefully checked the energy positions of the Mn t_{2g} band for the on-resonant Mn $2p$ - $3d$ valence band spectra obtained with incident photon energies C–G (spanning the Mn L_3 -edge main peak) shown in Fig. 8, and they are positioned at a BE of 2.0 ± 0.1 eV. This means the Mn^{3+} and Mn^{4+} t_{2g} states are degenerate. Comparing the on- and off-resonant Tb $3d$ - $4f$ spectra, it is understood that the ${}^8\text{S}_{7/2}$ component of the Tb $4f$ multiplets overlaps with the Mn $3d$ t_{2g} -derived feature at 2 eV BE. It is known from earlier work [80] on TbRh that the ${}^8\text{S}$ component of the Tb $4f$ multiplets does not show a strong enhancement in on-resonance spectra due to hybridization effects with Rh $4d$ states, while the (${}^6\text{H}, {}^6\text{G}, {}^6\text{I}$) character Tb final states are strongly enhanced on resonance. Similarly, the ${}^8\text{S}$ component hybridizes with the Mn $3d$ states in TSMO50 and does not show strong $3d$ - $4f$ resonance enhancement.

The band gap of TSMO50 was estimated using a linear extrapolation of the leading edge, as shown in the inset of Fig. 12. We use spectrum E to estimate this gap as it showed the highest intensity for the Mn^{3+} character e_g band on resonance. The energy separation between the valence band edge of TSMO50 and Fermi level is taken as an upper estimate of the band gap of TSMO50 in the occupied density of states, and the band gap was found to be < 100 meV. This result confirms that TSMO50 is a small-gap semiconductor, and given the lower energy resolution of the photoemission spectroscopy measurements, it is roughly consistent with the activation energy of 30–50 meV estimated from electrical measurements [31]. On the other hand, for the series $\text{La}_{0.67}\text{Pb}_{0.33}\text{Mn}_{1-x}\text{Fe}_x\text{O}_3$, Kowalik *et al.* used the same procedure to estimate the band gaps and reported values of ~ 1.7 to 2 eV, confirming the insulating behavior of the series [44].

Finally, based on all the experimental results and the electronic parameters obtained from calculation for the XAS and core level spectra, we have obtained a schematic description of the electronic structure of TSMO50, as shown in Fig. 13. Using the known band gap of insulating TbMnO_3 [~ 0.48 eV;

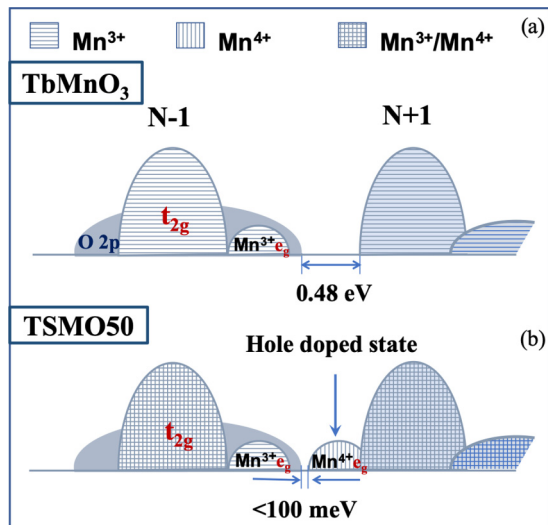


FIG. 13. Schematic description of the electronic structure of (a) pure TbMnO_3 and (b) TSMO50.

Fig. 13(a) [81], it is clear that TSMO50 becomes a small-gap semiconductor, with a gap of <100 meV. The strontium doping in TbMnO_3 leads to the formation of hole states, but it does not close the gap in TSMO50. TSMO50 is a charge transfer semiconductor with the on-site Coulomb energy U_{dd} being larger than the charge transfer Δ . In comparison, for transition metal fluorides MF_2 , the charge transfer Δ was estimated to vary from ~ 6 to 7 eV while the on-site Coulomb energy U_{dd} was estimated to vary from ~ 3 to 6 eV, indicating the fluorides are Mott-Hubbard systems with $U_{dd} < \Delta$ [82]. Further, the t_{2g} states of Mn^{3+} and Mn^{4+} are nearly degenerate, while the crystal field splitting for Mn^{3+} states is 1.6 eV and that for Mn^{4+} states is 2.5 eV, as estimated from the model calculations. This results in a gap essentially determined by the strongly hybridized occupied $\text{Mn}^{3+} - \text{O } 2p$ states and unoccupied $\text{Mn}^{4+} - \text{O } 2p$ states, as shown in Fig. 13.

IV. CONCLUSIONS

We studied the electronic structure of single-crystal $\text{Tb}_{0.5}\text{Sr}_{0.5}\text{MnO}_3$ using soft x-ray photoemission, hard x-ray

photoemission, x-ray absorption, and resonant photoemission spectroscopy. Core level photoemission and x-ray absorption spectroscopy combined with model calculations could be used to determine the valence states of Tb, Sr, and Mn ions in $\text{Tb}_{0.5}\text{Sr}_{0.5}\text{MnO}_3$. The spectral features could be explained by a 1:1 ratio of Mn^{3+} and Mn^{4+} states. Resonant photoemission spectroscopy across the Mn $2p$ - $3d$ threshold showed two distinct L_3VV two-hole correlation satellites which are attributed to the mainly Mn $3d^n$ and $3d^{n+1}\underline{L}^1$ states. We estimated on-site Coulomb energy $U_{dd} \sim 5.5 \pm 0.2$ eV, indicative of strong Coulomb correlations in the Mn $3d^n$ states. The O $1s$ - $2p$ resonant photoemission showed an O $2p$ two-hole correlation satellite, and U_{pp} was estimated to be $\sim 3.4 \pm 0.2$ eV for the O site. We also estimated intersite Coulomb energy $U_{pd} = 0.7 \pm 0.2$ eV from the $d^{n+1}\underline{L}^1$ correlation satellite. Valence band photoemission showed a small-gap semiconductor (< 100 meV) which is reduced compared to the parent TbMnO_3 (~ 0.48 eV). The estimated electronic structure parameters of the on-site Coulomb energies, the charge transfer energy, and the hybridization strength obtained from the model calculations indicate that $\text{Tb}_{0.5}\text{Sr}_{0.5}\text{MnO}_3$ can be described as a strongly correlated system with significant charge transfer character.

ACKNOWLEDGMENTS

A.C. thanks the Ministry of Science and Technology of Taiwan, Republic of China, for financially supporting this research under Contract No. MOST 108-2112-M-213-001-MY3. The synchrotron radiation experiments were performed at BL17SU, SPring-8, with the approval of RIKEN (Grant No. 20140019). J.R.-Z. and G.R.C. are grateful for financial support under Grant No. PIE201060E013 to the Spanish Ministry of Science and Innovation (MICINN; Ministerio de Ciencia e Innovación de España) and the Spanish National Research Council (CSIC; Consejo Superior de Investigaciones Científicas). The European Synchrotron Facility, MICINN, and CSIC are acknowledged for provision of synchrotron radiation facilities.

- [1] R. M. Kusters, J. Singleton, D. A. Keen, R. McGreevy, and W. Hayes, Magnetoresistance measurements on the magnetic semiconductor $\text{Nd}_{0.5}\text{Pb}_{0.5}\text{MnO}_3$, *Physica B (Amsterdam, Neth.)* **155**, 362 (1989).
- [2] K. Chahara, T. Ohno, M. Kasai, and Y. Kozono, Magnetoresistance in magnetic manganese oxide with intrinsic antiferromagnetic spin structure, *Appl. Phys. Lett.* **63**, 1990 (1993).
- [3] R. von Helmolt, J. Wecker, B. Holzapfel, L. Schultz, and K. Samwer, Giant Negative Magnetoresistance in Perovskitelike $\text{La}_{2/3}\text{Ba}_{1/3}\text{MnO}_x$ Ferromagnetic Films, *Phys. Rev. Lett.* **71**, 2331 (1993).
- [4] S. Jin, T. H. Tiefel, M. McCormack, R. A. Fastnacht, R. Ramesh, and L. H. Chen, Thousandfold change in resistiv-

ity in magnetoresistive La-Ca-Mn-O films, *Science* **264**, 413 (1994).

- [5] L. Sheng, D. Y. Xing, D. N. Sheng, and C. S. Ting, Theory of Colossal Magnetoresistance in $\text{R}_{1-x}\text{A}_x\text{MnO}_3$, *Phys. Rev. Lett.* **79**, 1710 (1997).
- [6] *Colossal Magnetoresistance Oxides*, edited by Y. Tokura (Gordon and Breach, New York, 2000).
- [7] N. Mannella, A. Rosenhahn, C. H. Booth, S. Marchesini, B. S. Mun, S.-H. Yang, K. Ibrahim, Y. Tomioka, and C. S. Fadley, Direct Observation of High-Temperature Polaronic Behavior in Colossal Magnetoresistive Manganites, *Phys. Rev. Lett.* **92**, 166401 (2004).
- [8] N. Mannella, C. H. Booth, A. Rosenhahn, B. C. Sell, A. Nambu, S. Marchesini, B. S. Mun, S.-H. Yang, M. Watanabe,

- K. Ibrahim, E. Arenholz, A. Young, J. Guo, Y. Tomioka, and C. S. Fadley, Temperature-dependent evolution of the electronic and local atomic structure in the cubic colossal magnetoresistive manganite $\text{La}_{1-x}\text{Sr}_x\text{MnO}_3$, *Phys. Rev. B* **77**, 125134 (2008).
- [9] H. Kawano, R. Kajimoto, H. Yoshizawa, Y. Tomioka, H. Kuwahara, and Y. Tokura, Magnetic Ordering and Relation to the Metal-Insulator Transition in $\text{Pr}_{1-x}\text{Sr}_x\text{MnO}_3$ and $\text{Nd}_{1-x}\text{Sr}_x\text{MnO}_3$ with $x \sim 1/2$, *Phys. Rev. Lett.* **78**, 4253 (1997).
- [10] K. Miyano, T. Tanaka, Y. Tomioka, and Y. Tokura, Photoinduced Insulator-to-Metal Transition in a Perovskite Manganite, *Phys. Rev. Lett.* **78**, 4257 (1997).
- [11] C. N. R. Rao, A. Arulraj, P. N. Santosh, and A. K. Cheetham, Charge-ordering in manganates, *Chem. Mater.* **10**, 2714 (1998).
- [12] C. N. R. Rao, Charge, spin, and orbital ordering in the perovskite manganates, $\text{Ln}_{1-x}\text{A}_x\text{MnO}_3$ (Ln=Rare Earth, A= Ca or Sr), *J. Phys. Chem. B* **104**, 5877 (2000).
- [13] G. H. Jonker, Magnetic compounds with perovskite structure IV conducting and non-conducting compounds, *Physica (Amsterdam)* **22**, 707 (1956).
- [14] *Crystallographic and Magnetic Properties of Perovskite and Perovskite-Related Compounds*, edited by J. B. Goodenough, J. M. Longo, and K. H. Hellwege, Landolt-Bornstein Tables, New Series III Vol. 4a (Springer, Berlin, 1970), p. 126.
- [15] Z. Huang, Y. Cao, Y. Sun, Y. Xue, and C. Chu, Coupling between the ferroelectric and antiferromagnetic orders, *Phys. Rev. B* **56**, 2623 (1997).
- [16] B. Dabrowski, S. Kolesnik, A. Baszczuk, O. Chmaissem, T. Maxwell, and J. Mais, Structural, transport, and magnetic properties of RMnO_3 perovskites ($R = \text{La, Pr, Nd, Sm, }^{153}\text{Eu, Dy}$), *J. Solid State Chem.* **178**, 629 (2005).
- [17] J. S. Zhou, J. B. Goodenough, J. M. Gallardo-Amores, E. Morn, M. A. Alario-Franco, and R. Caudillo, Hexagonal versus perovskite phase of manganite RMnO_3 ($R = \text{Y, Ho, Er, Tm, Yb, Lu}$), *Phys. Rev. B* **74**, 014422 (2006).
- [18] B. H. Kim and B. I. Min, Nearest and next-nearest superexchange interactions in orthorhombic perovskite manganites RMnO_3 ($R = \text{rare earth}$), *Phys. Rev. B* **80**, 064416 (2009).
- [19] A. Marthinsen, C. Faber, U. Aschauer, N. A. Spaldin, and S. M. Selbach, Coupling and competition between ferroelectricity, magnetism, strain, and oxygen vacancies in AMnO_3 perovskites, *MRS Commun.* **6**, 182 (2016).
- [20] L. P. Gor'kov and V. Z. Kresin, Mixed-valence manganites: Fundamentals and main properties, *Phys. Rep.* **400**, 149 (2004).
- [21] G. H. Jonker and J. H. Van Santen, Ferromagnetic compounds of manganese with perovskite structure, *Physica (Amsterdam)* **16**, 337 (1950).
- [22] P. Schiffer, A. P. Ramirez, W. Bao, and S.-W. Cheong, Low Temperature Magnetoresistance and the Magnetic Phase Diagram of $\text{La}_{1-x}\text{Ca}_x\text{MnO}_3$, *Phys. Rev. Lett.* **75**, 3336 (1995).
- [23] J. C. Loudon, N. D. Mathur, and P. A. Midgley, Charge ordered ferromagnetic phase in $\text{La}_{0.5}\text{Ca}_{0.5}\text{MnO}_3$, *Nature (London)* **420**, 797 (2002).
- [24] S. S. Kekade, R. S. Devan, A. V. Deshmukh, D. M. Phase, R. J. Choudhary, and S. I. Patil, Electron transport behavior and charge ordering phenomena in electron transport behavior and charge ordering phenomena in $\text{La}_{0.5}\text{Ca}_{0.5}\text{MnO}_3$, *J. Alloys Compd.* **682**, 447 (2016).
- [25] F. Damay, A. Maignan, C. Martin, and B. Raveau, Cation size-temperature phase diagram of the manganites $\text{Ln}_{0.5}\text{Sr}_{0.5}\text{MnO}_3$, *J. Appl. Phys.* **81**, 1372 (1997).
- [26] X. Zhang, J. Fan, L. Xu, D. Hu, W. Zhang, and Y. Zhu, Magnetic and magnetocaloric properties of nanocrystalline $\text{La}_{0.5}\text{Sr}_{0.5}\text{MnO}_3$, *Ceram. Int.* **42**, 1476 (2016).
- [27] Y. Hiramitsu, K. Yoshii, Y. Yoneda, J. Mizuki, A. Nakamura, Y. Shimojo, Y. Ishii, Y. Morii, and N. Ikeda, Magnetic and dielectric properties of $\text{Tb}_{0.5}\text{Ca}_{0.5}\text{MnO}_3$, *Jpn. J. Appl. Phys.* **46**, 7171 (2007).
- [28] T. Wu and P. Gao, Development of perovskite-type materials for thermoelectric application, *Materials* **11**, 999 (2018).
- [29] J. M. Chen, T. L. Chou, J. M. Lee, S. A. Chen, T. S. Chan, T. H. Chen, K. T. Lu, W. T. Chuang, H.-S. Sheu, S. W. Chen, C. M. Lin, N. Hiraoka, H. Ishii, K. D. Tsuei, and T. J. Yang, Pressure-induced structural distortion of TbMnO_3 : A combined x-ray diffraction and x-ray absorption spectroscopy study, *Phys. Rev. B* **79**, 165110 (2009).
- [30] K. Yoshii, Y. Hiramitsu, Y. Yoneda, Y. Okajima, Y. Nishihata, J. Mizuki, and N. Ikeda, Magnetic and dielectric study of $\text{R}_{0.5}\text{Sr}_{0.5}\text{MnO}_3$ ($R = \text{Gd, Tb and Dy}$), *Mater. Res. Bull.* **45**, 1574 (2010).
- [31] H. Nhalil and S. Elizabeth, Signatures of correlation between magnetic and electrical properties of $\text{Tb}_{0.5}\text{Sr}_{0.5}\text{MnO}_3$ single crystals, *Europhys. Lett.* **116**, 57006 (2016).
- [32] E. Stavitski and F. M. F. de Groot, The CTM4XAS program for EELS and XAS spectral shape analysis of transition metal L edges, *Micron* **41**, 687 (2010).
- [33] K. Horiba, N. Kamakura, K. Yamamoto, K. Kobayashi, and S. Shin, A high-resolution angle-resolved photoemission spectrometer combined with laser molecular-beam epitaxy at SPring-8 BL17SU, *J. Electron Spectrosc. Relat. Phenom.* **144–147**, 1027 (2005).
- [34] H. Ohashi *et al.*, Performance of a highly stabilized and high-resolution beamline BL17SU for advanced soft x-ray spectroscopy at SPring-8, in *Synchrotron Radiation Instrumentation: Ninth International Conference on Synchrotron Radiation Instrumentation*, edited by J.-Y. Choi and S. Rah, AIP Conf. Proc. No. 879 (AIP, Melville, NY, 2007), p. 523.
- [35] F. Parmigiani and L. Sangaletti, Fine structures in the X-ray photoemission spectra of MnO , FeO , CoO , and NiO single crystals, *J. Electron Spectrosc. Relat. Phenom.* **98–99**, 287 (1999).
- [36] L. Q. Wu, Y. C. Li, S. Q. Li, Z. Z. Li, G. D. Tang, W. H. Qi, L. C. Xue, X. S. Ge, and L. L. Ding, Method for estimating ionicities of oxides using O 1s photoelectron spectra, *AIP Adv.* **5**, 097210 (2015).
- [37] A. Chainani, M. Mathew, and D. D. Sarma, Electron spectroscopic investigation of the semiconductor-metal transition in $\text{La}_{1-x}\text{Sr}_x\text{MnO}_3$, *Phys. Rev. B* **47**, 15397 (1993).
- [38] T. Saitoh, A. E. Bocquet, T. Mizokawa, H. Namatame, and A. Fujimori, Electronic structure of $\text{La}_{1-x}\text{Sr}_x\text{MnO}_3$ studied by photoemission and x-ray-absorption spectroscopy, *Phys. Rev. B* **51**, 13942 (1995).
- [39] K. Horiba *et al.*, Nature of the Well Screened State in Hard X-Ray Mn 2p Core-Level Photoemission Measurements of $\text{La}_{1-x}\text{Sr}_x\text{MnO}_3$ Films, *Phys. Rev. Lett.* **93**, 236401 (2004).
- [40] T. Hishida, K. Ohbayashi, M. Kobata, E. Ikenaga, T. Sugiyama, K. Kobayashi, M. Okawa, and T. Saitoh, Empirical relationship between x-ray photoemission spectra and electrical conductivity in a colossal magnetoresistive manganite $\text{La}_{1-x}\text{Sr}_x\text{MnO}_3$, *J. Appl. Phys.* **113**, 233702 (2013).

- [41] *Photoelectron Spectroscopy: Bulk and Surface Electronic Structures*, edited by S. Suga and A. Sekiyama (Springer, New York, 2014).
- [42] F. M. F. de Groot, Multiplet effects in X-ray spectroscopy, *Coord. Chem. Rev.* **249**, 31 (2005).
- [43] F. M. F. de Groot and A. Kotani, *Core Level Spectroscopy of Solids* (CRC Press, Boca Raton, FL, 2008).
- [44] M. Kowalik, R. Zalecki, and A. Kolodziejczyk, Electronic states of colossal magnetoresistive manganites $La_{0.67}Pb_{0.33}Mn_{1-x}Fe_xO_3$ from photoemission spectroscopy, *Acta Phys. Pol. A* **117**, 277 (2010).
- [45] M. Kowalik, M. Sikora, R. Zalecki, A. Kolodziejczyk, and Cz. Kapusta, XANES and X-ray photoemission of the $La_{0.67}(Ca, Pb)_{0.33}Mn_{1-x}Fe_xO_3$ compounds, *Radiat. Phys. Chem.* **80**, 1068 (2011).
- [46] R. Zalecki, A. Kolodziejczyk, Cz. Kapusta, and K. Krop, Electronic states of $La_{1-x}Ca_xMnO_3$ from photoelectron spectroscopy, *J. Alloys Compd.* **328**, 175 (2001).
- [47] W. T. Hong, K. A. Stoerzinger, B. Moritz, T. P. Devereaux, W. Yang, and Y. Shao-Horn, Probing $LaMO_3$ metal and oxygen partial density of states using X-ray emission, absorption, and photoelectron spectroscopy, *J. Phys. Chem. C* **119**, 2063 (2015).
- [48] F. Offi, N. Mannella, T. Pardini, G. Panaccione, A. Fondacaro, P. Torelli, M. W. West, J. F. Mitchell, and C. S. Fadley, Temperature-dependent electronic structure of the colossal magnetoresistive manganite $La_{0.7}Sr_{0.3}MnO_3$ from hard x-ray photoemission, *Phys. Rev. B* **77**, 174422 (2008).
- [49] T. Pincelli *et al.*, Quantifying the critical thickness of electron hybridization in spintronics materials, *Nat. Commun.* **8**, 16051 (2017).
- [50] J. Rubio-Zuazo *et al.* (unpublished).
- [51] J. Lee, B. Kim, B. H. Kim, B. I. Min, S. Kolesnik, O. Chmaissem, J. Mais, and B. Dabrowski, H. J. Shin, D. H. Kim, H. J. Lee, and J.-S. Kang, Valence-state transition in $SrMn_{1-x}Mo_xO_3$ ($0 < x < 0.5$) investigated by soft x-ray absorption spectroscopy, *Phys. Rev. B* **80**, 205112 (2009).
- [52] K. Mitsuhashi, Y. Kitsudo, H. Matsumoto, A. Visikovskiy, M. Takizawa, T. Nishimura, T. Akita, and Y. Kido, Electronic charge transfer between Au nano-particles and TiO_2 -terminated $SrTiO_3$ (001) substrate, *Surf. Sci.* **604**, 548 (2010).
- [53] O. Zeybek, The magnetic behaviour of the surface and bulk components of $Tb(0001)$ films, *Turk J. Phys.* **29**, 319 (2006).
- [54] J.-S. Kang, J. H. Kim, A. Sekiyama, S. Kasai, S. Suga, S. W. Han, K. H. Kim, E. J. Choi, T. Kimura, T. Muro, Y. Saitoh, C. G. Olson, J. H. Shim, and B. I. Min, Resonant photoemission spectroscopy study of impurity-induced melting in Cr- and Ru-doped $Nd_{1/2}A_{1/2}MnO_3$ ($A = Ca, Sr$), *Phys. Rev. B* **68**, 012410 (2003).
- [55] J.-H. Park, S.-W. Cheong, and C. T. Chen, Double-exchange ferromagnetism in $La(Mn_{1-x}Co_x)O_3$, *Phys. Rev. B* **55**, 11072 (1997).
- [56] M. Finazzi, N. B. Brookes and F. M. F. de Groot, $2p3s3p$, $2p3p3p$, and $2p3s3s$ resonant Auger spectroscopy from NiO, *Phys. Rev. B* **59**, 9933 (1999).
- [57] M. Cini, Density of state of two interacting holes in a solid, *Solid State Commun.* **20**, 605 (1976).
- [58] M. Cini, Two hole resonances in the XVV Auger spectra of solids, *Solid State Commun.* **24**, 681 (1977).
- [59] G. A. Sawatzky, Quasiatomic Auger Spectra in Narrow-Band Metals, *Phys. Rev. Lett.* **39**, 504 (1977).
- [60] M. Cini, Comment on quasiatomic Auger spectra in narrow-band metals, *Phys. Rev. B* **17**, 2788 (1978).
- [61] M. Cini, Theory of the Auger effect in solids: Plasmon effects in electron spectroscopies of valence states, *Phys. Rev. B* **17**, 2486 (1978).
- [62] S. Hufner, S.-H. Yang, B. S. Mun, C. S. Fadley, J. Schafer, E. Rotenberg, and S. D. Kevan, Observation of the two-hole satellite in Cr and Fe metal by resonant photoemission at the $2p$ absorption energy, *Phys. Rev. B* **61**, 12582 (2000).
- [63] P. Werner, R. Sakuma, F. Nilsson, and F. Aryasetiawan, Dynamical screening in La_2CuO_4 , *Phys. Rev. B* **91**, 125142 (2015).
- [64] G. A. Sawatzky and D. Post, X-ray photoelectron and Auger spectroscopy study of some vanadium oxides, *Phys. Rev. B* **20**, 1546 (1979).
- [65] A. Chainani, M. Mathew, and D. D. Sarma, Electron-spectroscopy study of the semiconductor-metal transition in $La_{1-x}Sr_xCoO_3$, *Phys. Rev. B* **46**, 9976 (1992).
- [66] A. Chainani, M. Mathew, and D. D. Sarma, Electronic structure of $La_{1-x}Sr_xFeO_3$, *Phys. Rev. B* **48**, 14818 (1993).
- [67] S. Johnston, A. Mukherjee, I. Elfimov, M. Berciu, and G. A. Sawatzky, Charge Disproportionation Without Charge Transfer in the Rare-Earth-Element Nickelates as a Possible Mechanism for the Metal-Insulator Transition, *Phys. Rev. Lett.* **112**, 106404 (2014).
- [68] Y. Ishida, R. Eguchi, M. Matsunami, K. Horiba, M. Taguchi, A. Chainani, Y. Senba, H. Ohashi, H. Ohta, and S. Shin, Coherent and Incoherent Excitations of Electron-Doped $SrTiO_3$, *Phys. Rev. Lett.* **100**, 056401 (2008).
- [69] D. Van der Marel, J. van Elp, and D. G. A. Sawatzky, X-ray photoemission, bremsstrahlung isochromat, Auger-electron, and optical spectroscopy studies of Y-Ba-Cu-O thin films, *Phys. Rev. B* **37**, 5136 (1988).
- [70] A. Balzarotti, M. De Crescenzi, N. Motta, F. Patella, and A. Sgarlata, Valence charge fluctuations in $YBa_2Cu_3O_{7-\delta}$ from core-level spectroscopies, *Phys. Rev. B* **38**, 6461 (1988).
- [71] A. Fujimori, E. Takayama-Muromachi, Y. Uchida, and B. Okai, Spectroscopic evidence for strongly correlated electronic states in La-Sr-Cu and Y-Ba-Cu oxides, *Phys. Rev. B* **35**, 8814 (1987).
- [72] M. Imada, A. Fujimori, and Y. Tokura, Metal-insulator transition, *Rev. Mod. Phys.* **70**, 1039 (1998).
- [73] A. Amaricci, A. Camjayi, K. Haule, G. Kotliar, D. Tanaskovi, and V. Dobrosavljević, Extended Hubbard model: Charge ordering and Wigner-Mott transition, *Phys. Rev. B* **82**, 155102 (2010).
- [74] K. Kacpica, W. Klobus, and S. Robaszkiewicz, Interplay between charge and magnetic orderings in the zero-bandwidth limit of the extended Hubbard model for strong on-site repulsion, *Acta Phys. Pol. A* **121**, 1032 (2012).
- [75] A. Chainani, M. Sicot, Y. Fagot-Revurat, G. Vasseur, J. Granet, B. Kierren, L. Moreau, M. Oura, A. Yamamoto, Y. Tokura, and D. Malterre, Evidence for Weakly Correlated Oxygen Holes in the Highest- T_c Cuprate Superconductor $HgBa_2Ca_2Cu_3O_{8+\delta}$, *Phys. Rev. Lett.* **119**, 057001 (2017).
- [76] D. K. G. de Boer, C. Haas, and G. A. Sawatzky, Auger spectra of compounds of Sc, Ti and Cr, *J. Phys. F: Met. Phys.* **14**, 2769 (1984).

- [77] J. M. Chen, Z. Hu, H. T. Jeng, Y. Y. Chin, J. M. Lee, S. W. Huang, K. T. Lu, C. K. Chen, S. C. Haw, T. L. Chou, H.-J. Lin, C. C. Shen, R. S. Liu, A. Tanaka, L. H. Tjeng, and C. T. Chen, Strong orbital polarization in orthorhombic DyMnO₃: A combined x-ray linear dichroism and *ab initio* electronic structure study, *Phys. Rev. B* **81**, 201102(R) (2010).
- [78] J. K. Lang, Y. Baer, and P. A. Cox, Study of the 4f and valence band density of states in rare-earth metals. II. Experiment and results, *J. Phys. F: Met. Phys.* **11**, 121 (1981).
- [79] F. Gerken, Calculated photoemission spectra of the 4f states in the rare-earth metals, *J. Phys. F: Met. Phys.* **13**, 703 (1983).
- [80] S. L. Molodtsov, Yu. Kucherenko, D. V. Vyalikh, G. Behr, A. Starodubov, and C. Laubschat, Strong hybridization of 4f states of heavy rare earths in intermetallic compounds, *Phys. Rev. B* **68**, 193101 (2003).
- [81] L. G. Cai, F. M. Liu, and W. W. Zhong, Structural, electronic and optical properties of orthorhombic distorted perovskite TbMnO₃, *Chin. Phys. B* **19**, 097101 (2010).
- [82] J. Jiménez-Miera, P. Olalde-Velasco, G. Herrera-Pérez, G. Carabalí-Sandoval, E. Chavirac, W.-L. Yang, and J. Denlinger, Strongly correlated transition metal compounds investigated by soft X-ray spectroscopies and multiplet calculations, *J. Electron Spectrosc. Relat. Phenom.* **196**, 136 (2014).